Letter

Bridging necking and shear-banding mediated tensile failure in glasses

David Richard,[1,*] Ethen Thomas Lund,[2,*] Jan Schroers,[2,†] and Eran Bouchbinder[3,‡]

[1]*Université Grenoble Alpes, CNRS, LIPhy, 38000 Grenoble, France*

[2]*Department of Mechanical Engineering and Materials Science, Yale University, New Haven, Connecticut 06520, USA*

[3]*Chemical and Biological Physics Department, Weizmann Institute of Science, Rehovot 7610001, Israel*

(Received 20 December 2022; accepted 23 February 2023; published 10 March 2023)

The transition between necking-mediated tensile failure of glasses, at elevated temperatures and/or low strain rates, and shear-banding-mediated tensile failure, at low temperatures and/or high strain rates, is investigated using tensile experiments on metallic glasses and atomistic simulations. We experimentally and simulationally show that this transition occurs through a sequence of macroscopic failure patterns, parametrized by the ultimate tensile strength. Quantitatively analyzing the spatiotemporal dynamics preceding failure, using large scale atomistic simulations corroborated by experimental fractography, reveals how the collective evolution and mutual interaction of shear-driven plasticity and dilation-driven void formation (cavitation) control the various macroscopic failure modes. In particular, we find that, at global failure, the size of the largest cavity in the loading direction exhibits a nonmonotonic dependence on the temperature at a fixed strain rate, which is rationalized in terms of the interplay between shear- and dilation-driven plasticity. We also find that the size of the largest cavity scales with the cross-sectional area of the undeformed sample. Our results shed light on tensile failure of glasses and highlight the need to develop elastoplastic constitutive models of glasses incorporating both shear- and dilation-driven irreversible processes.

DOI: 10.1103/PhysRevMaterials.7.L032601

Glasses subjected to sufficiently large tensile stresses, like any other materials, inevitably fail. At elevated temperatures and/or low strain rates, deformation is essentially homogeneous and failure is known to be mediated by necking [1,2], where spatially extended plastic deformation geometrically localizes at a radially symmetric, shrinking cross-sectional area [3,4]. At low temperatures and/or high strain rates, deformation is highly localized and failure is mediated by shear banding [1], where plastic deformation strongly localizes at an oblique (symmetry-breaking) plane, before transforming into a catastrophic crack [3,4]. While progress has been made in understanding these two end members of tensile failure modes of glasses, our understanding of the transition between them as a function of the temperature and strain-rate significantly lags behind. In this study, using tensile experiments performed on well-controlled metallic glasses and large-scale molecular dynamics simulations of model glasses, we investigate the transition between necking- and shear-banding-mediated tensile failure in glasses. We focus both on the macroscopic tensile failure patterns and on the spatiotemporal elastoplastic dynamics that accompany them, paying special attention to the interplay between shear-driven plasticity and dilation-driven void formation (cavitation) [5–9].

We performed uniaxial tension tests on cylindrical rods made of a $Zr_{44}Ti_{11}Cu_{10}Ni_{10}Be_{25}$ metallic glass ($T_g = 625$ K) of diameter $D_0 = 1.8$ mm, over a range of temperatures T and strain rates $\dot{\epsilon}$. The rods were prepared such that the as-cast state is statistically similar between samples (i.e., featuring the same fictive temperature [10]), see Supplemental Material for details [11], ensuring that all of the observed variations in the failure dynamics are due to variations in the control parameters T and $\dot{\epsilon}$, and not different nonequilibrium histories. The rods were clamped in a universal testing machine and maintained at a temperature T (both below and above T_g, in the range of $T = 529$–659 K), before being loaded in tension at a strain rate $\dot{\epsilon}$ (in the range $\dot{\epsilon} = 0.2$–1.3 s^{-1}); see [11] for details.

For any uniaxial test with prescribed T and $\dot{\epsilon}$, we measured the applied stress σ as a function of the strain ϵ. For each stress-strain curve $\sigma(\epsilon)$, we extracted the peak value, i.e., the ultimate tensile strength (UTS), $\sigma_{\rm UTS}$. In Fig. 1(a), we present the observed macroscopic, postmortem failure patterns as a function of increasing $\sigma_{\rm UTS}$, independent of whether its variation has been achieved by varying T or $\dot{\epsilon}$. At small $\sigma_{\rm UTS}$, corresponding to high T and low $\dot{\epsilon}$, necking-mediated failure is observed. At large $\sigma_{\rm UTS}$, corresponding to low T and high $\dot{\epsilon}$, oblique, shear-banding-mediated failure is observed. In between, a sequence of macroscopic failure patterns is observed, apparently parametrized by $\sigma_{\rm UTS}$.

We roughly identify three intermediate failure patterns, sketched on the top row of Fig. 1(b), between necking-mediated failure (leftmost) and shear-banding-mediated failure (rightmost). To better describe and understand the sequence of observed macroscopic failure patterns, we polished the postmortem samples that feature a vanishingly small cross section at failure—characterizing predominantly necking-mediated failure [the two leftmost sketches on the top row of Fig. 1(b)]—along the rod's long axis and imaged it using a scanning electron microscope (see [11] for details).

*These authors contributed equally to this work.

†jan.schroers@yale.edu

‡eran.bouchbinder@weizmann.ac.il

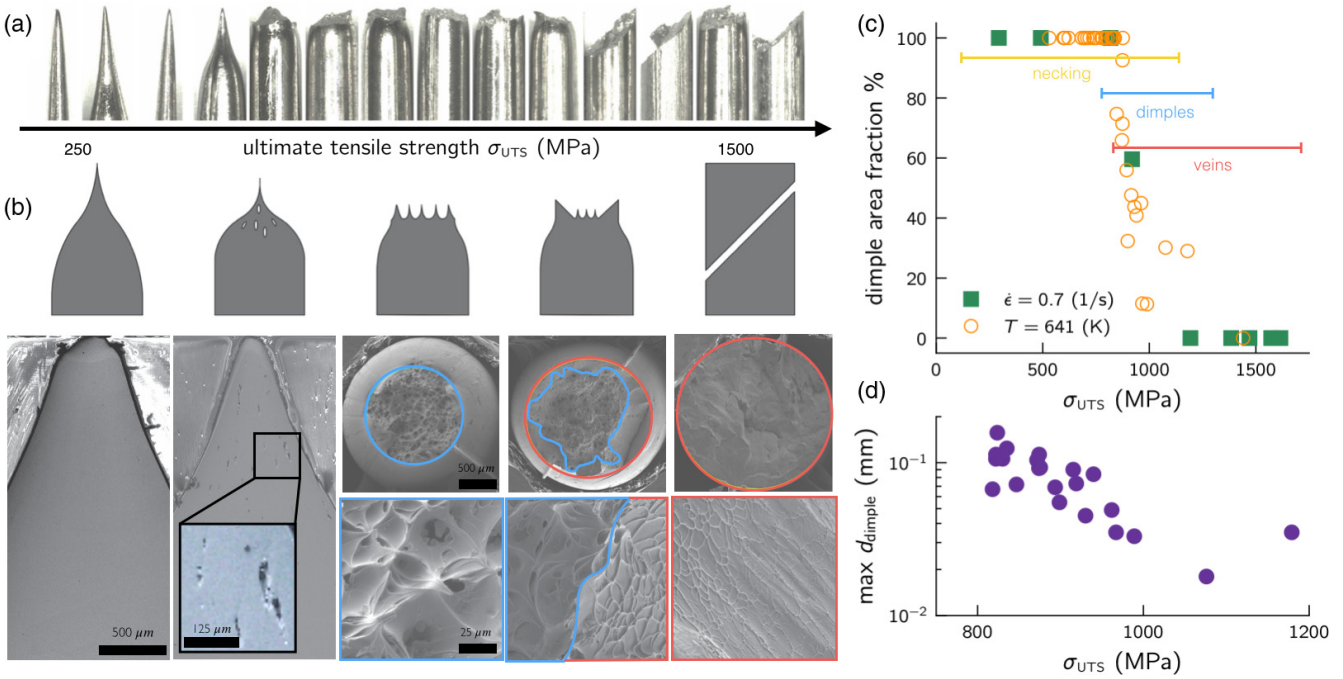

FIG. 1. (a) Side view of the tensile samples after failure sorted by increasing ultimate tensile strength σ_{UTS}, which is varied either by varying T or $\dot{\epsilon}$. σ_{UTS} varies by roughly a factor of 6.5, approximately from 250 MPa to 1600 MPa as indicated, but note that the presented samples are not placed at equal σ_{UTS} intervals. (b) Sketches of the macroscopic failure modes (top row), ranging from necking-mediated failure on the left (low σ_{UTS}, corresponding to high T or low $\dot{\epsilon}$) to shear-banding-mediated failure of the right (high σ_{UTS}, corresponding to low T or high $\dot{\epsilon}$); see text for details. (Bottom row) Vertical sample polishing (two leftmost parts) and fractographic images (the rest), corresponding to the sketches above (scale bars are added); see extensive discussion in the text. The stated scale bars apply to each set of adjacent micrographs, respectively. (c) Dimple area fraction vs σ_{UTS}, for a fixed $\dot{\epsilon}$ and varying T (green squares) and a fixed T and varying $\dot{\epsilon}$ (orange circles); see legend. The range of observed necking, dimples, and veins is indicated by horizontal colored bars. (d) The maximum dimple size vs σ_{UTS} for 800–1200 MPa, the range over which dimples are observed on the fracture surface [see also panel (c)].

For the lowest σ_{UTS}, where the neck is long, the bulk of the sample is homogeneous [see leftmost image on the bottom row of Fig. 1(b)], not revealing clear mesoscale structures and hence indicating homogeneous plastic deformation. At somewhat larger σ_{UTS}, for which samples still neck (yet the neck is shorter), the bulk of the sample reveals mesoscopic structures in the form of cavities [see the bottom row of Fig. 1(b) and the inset therein], indicating void formation and coalescence that leads to mesoscopic cavities in the bulk.

For postmortem samples that feature a finite cross section at failure, corresponding to the three rightmost sketches on the top row of Fig. 1(b), we imaged the fracture surfaces using a scanning electron microscope and performed a fractographic analysis. We identified two distinct fractographic patterns [10,12–17]: veins that are characteristic of localized shear plasticity and dimples that are characteristic of cavities. For intermediate σ_{UTS}, necking interrupted by cuplike structures appears in the macroscopic failure pattern [middle sketch on the top row of Fig. 1(b)], which corresponds to dimples covering the entire fracture surface; see the two images below the middle sketch on the top row of Fig. 1(b), where the blue boundary encircles dimples (here the entire surface). For yet higher σ_{UTS}, a cup-and-cone-like macroscopic pattern emerges [next-to-rightmost sketch on the top row of Fig. 1(b)], which corresponds to the coexistence of veinlike patterns at the periphery ("cone" part; see red encircling lines in the two images below) and dimples at the center ("cup" part; see blue encircling lines therein). Finally, for shear-banding-mediated failure at high σ_{UTS}, shown on the rightmost part of Fig. 1(b), veinlike patterns dominate the fracture surface.

The experimental results discussed above indicate that the various observed macroscopic failure modes emerge from the interplay between shear-driven plasticity and dilation-driven void formation/cavitation. These irreversible processes manifest themselves on the fracture surface, respectively, but generally also take place inside the bulk of the glass. To further quantify the fractographic manifestations of these irreversible processes, we present in Fig. 1(c) the percentage of the fractured area that is covered by dimples [see also panel (b)] as a function of σ_{UTS}, controlled either by varying $\dot{\epsilon}$ for a fixed T (orange circles) or by varying T at a fixed $\dot{\epsilon}$ (green squares); see the legend. While for small σ_{UTS} the dimple fraction is 100% by construction (it is simply the tip of the neck, which involves intensive plastic deformation), at higher σ_{UTS} the fraction drops, corresponding to the coexistence of dimples and veinlike patterns, until the latter dominate at the highest σ_{UTS}. Interestingly, the two curves appear to overlap, further substantiating the central role played by $\sigma_{UTS}(\dot{\epsilon}, T)$. Finally, in Fig. 1(d) we present the maximal dimple size vs $\sigma_{UTS} > 800$ MPa (on a log-linear scale), revealing a decreasing function.

The experiments described above span the entire spectrum of tensile failure modes in a glass as a function of a continuous control parameter and provide insight into the deformation

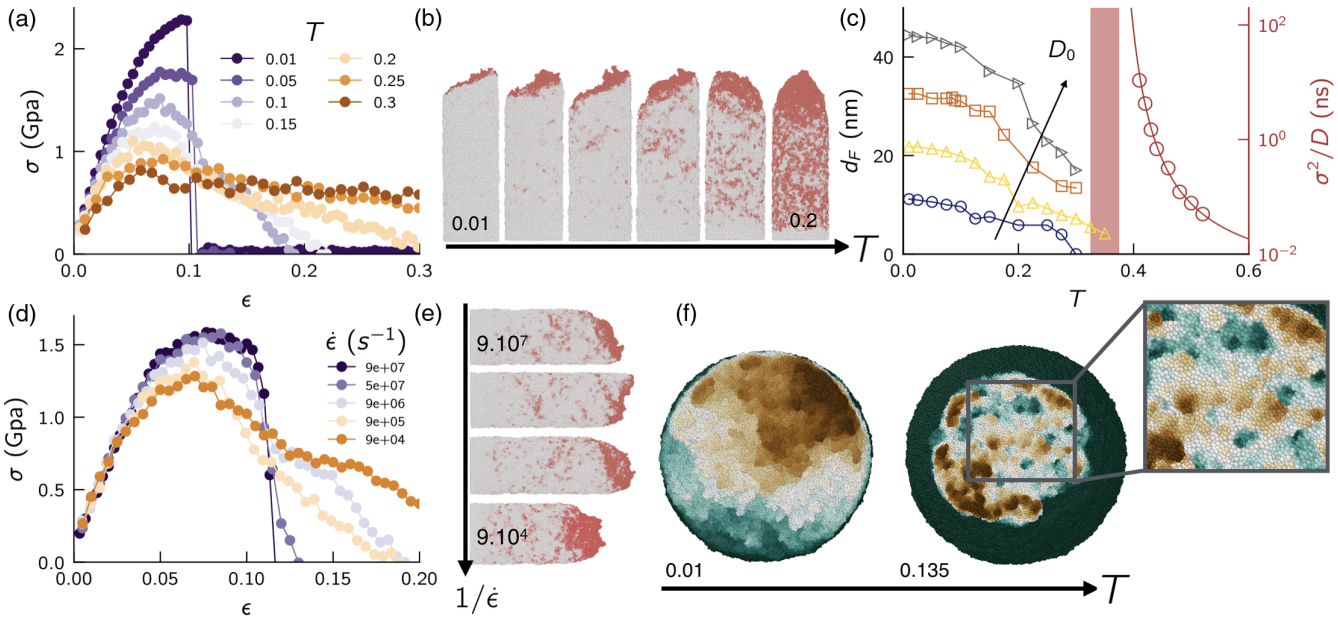

FIG. 2. (a) $\sigma(\epsilon)$ for various T's and a fixed $\dot{\epsilon} = 9 \times 10^6$ s^{-1}, with $D_0 = 11.8$ nm (all in simulational units; see [11]). (b) Postmortem global failure patterns for various T's (red particles represent shear-driven plasticity; see [11]). (c) Rod's diameter at failure d_F (left y axis) for various D_0's and the relaxation time σ^2/D (right y axis; the solid line is a Vogel-Fulcher-Tammann fit) vs T; see text for discussion. The red vertical bar provides an estimate for the computer glass transition. (d),(e) The same as panels (a),(b), but for various $\dot{\epsilon}$'s and a fixed $T = 0.1$. (f) Fractography at two different temperatures ($T = 0.01$ and 0.135) for $D_0 = 23.5$ nm and $\dot{\epsilon} = 5 \times 10^7$ s^{-1}, where the colors represent the depth from green to brown. A zoom in indicates small dimples.

processes involved. Yet, they offer only indirect evidence for the spatiotemporal dynamics that actually determine failure. To start closing this gap, we performed large-scale molecular dynamics simulations of tensile failure of computer glasses, over a wide range of temperatures and strain rates, allowing access to atomistic deformation processes preceding failure inside the glass. We employed computer glasses composed of a 50:50 binary mixture of particles interacting through a modified Lennard-Jones type potential [18] (see [11] for the rationale behind this choice), forming cylindrical rods of length $L_0 = 35.3$ nm and various diameters $D_0 =$ 11.8, 23.5, 35.3, and 47 nm (see [11] for unit conversion rules). The latter correspond to a number of particles N ranging from 300 K to 5 M. In order to minimize surface effects, we followed the casting procedure of [19]. Tensile test simulations were carried out using a massively parallel LAMMPS package [20], and details regarding the tensile loading and thermostatting procedures are provided in [11].

While atomistic simulations offer unique and powerful possibilities to resolve the spatiotemporal dynamics on the way to material failure, they are still limited in size and accessible timescales compared to macroscopic glasses (though the employed temperature range is fully consistent with laboratory experiments, including those reported in Fig. 1). For example, the lowest strain rate probed in our simulations is about 10^5 s^{-1}, significantly larger than in typical experiments. Consequently, our first goal is to understand whether atomistic simulations can recover the sequence of experimental failure modes presented in Fig. 1(a), albeit over different length and timescales. In Fig. 2(a), we present stress-strain curves $\sigma(\epsilon)$ for computer tensile tests performed on rods of diameter $D_0 = 11.8$ nm, over a broad range of T's at a fixed $\dot{\epsilon}$. The corresponding failure modes are presented in Fig. 2(b), where the red regions indicate shear-driven plasticity. The results clearly demonstrate that our atomistic simulations span the entire range of the experimentally observed failure modes, from oblique, shear-banding-mediated failure at low T to necking-mediated failure at higher T. These encouraging results give hope that atomistic simulations can offer fundamental insight into the spatiotemporal physics that accompany glass failure.

At the same time, as stressed above, the computer rods are much smaller than the experimental ones, and it is established that small glass samples exhibit enhanced plasticity compared to their macroscopic counterparts [21–26]. Consequently, we expect computer samples to exhibit necking-mediated failure at temperatures that are smaller than the corresponding ones for laboratory samples, when measured relative to the glass temperature T_g. For the experimental results of Fig. 1(a), necking-mediated failure emerges for $T > T_g$. In Fig. 2(c) (right y axis), we first estimate T_g for the computer samples by plotting the inverse diffusion coefficient (providing a measure of the structural relaxation time) as a function of T. By estimating the divergence of the relaxation time (solid line going through the red circles), we estimate the computer glass temperature as $T_g \simeq 0.35$ (in simulational units), marked by the red vertical bar.

In Fig. 2(c) (left y axis), we also plot the rod's diameter at failure, d_F, as a function of T for different initial rod's diameters D_0. The limit $d_F \to 0$ corresponds to the necking limit, i.e., to a vanishingly small cross section at failure. For the smallest D_0 [$D_0 = 11.8$ nm, blue circles, corresponding to the results shown in Figs. 2(a) and 2(b)], the necking limit is reached for $T < T_g$, unlike the laboratory experiments. With increasing D_0 [see arrow; different values of D_0 correspond

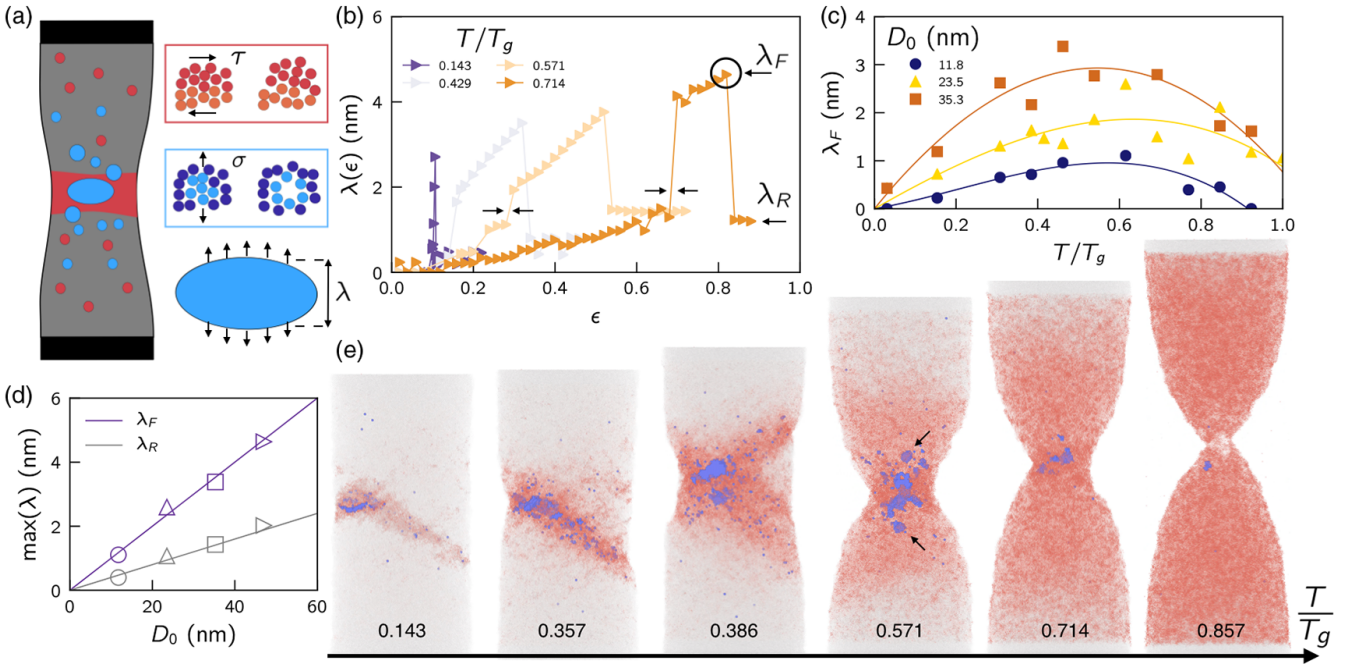

FIG. 3. (a) Sketch of a deformed rod, where shear-driven plasticity and voids are rendered in red and blue, respectively (see [11] for details). (b) The largest cavity size λ in the tensile direction vs ϵ for various T's, $\dot{\epsilon} = 5 \times 10^7$ s^{-1}, and $D_0 = 47$ nm. See text for discussion, including the meaning of the black circle and various arrows. λ_F and λ_R denote the values of λ at and after global failure, respectively. (c) λ_F vs T/T_g for various rod's diameters D_0 (see legend). See text for extensive discussion. (d) λ_F and λ_R vs D_0 (see legend). The solid lines indicate a linear behavior. (e) Side view snapshots at failure for various T/T_g (as indicated), with $D_0 = 23.5$ nm. The arrows in the $T/T_g = 0.571$ case indicate residual cavities inside the bulk.

to different symbols and colors in Fig. 2(c)], the necking limit is pushed to higher T's, clearly above T_g (while the actual $d_F \to 0$ limit is not fully resolved due to computational power constraints), making it consistent with the experimental observations.

In Figs. 2(d) and 2(e), we present results indicating that a similar sequence of failure modes [shown in Figs. 2(a) and 2(b)] is observed in our simulations for a fixed T and variable $\dot{\epsilon}$, in line with the experimental results presented in Fig. 1. In view of this correspondence, we focus on the variation with T hereafter. It is important to note that, in the snapshots presented in Figs. 2(b) and 2(e), we marked shear-driven plasticity (in red), but did not visualize dilation-driven plasticity in the form of void formation (to be considered below). In Fig. 2(f), we present the fractography of $D_0 = 23.5$ nm rods at two temperatures (one in the predominantly shear-banding-mediated failure regime, left, and the other in the predominantly "cup" failure regime, right); see figure caption for details. Small dimples are observed, as highlighted in the zoom in on the right, which are reminiscent of the experimental fractographic observation of Fig. 1(b) (middle part), though on much smaller length scales.

It is important to note, however, that we do not observe veinlike patterns during shear banding in our simulations. Veins are commonly attributed to meniscus instabilities caused by a local increase of the temperature and the accompanying reduced viscosity inside the shear band [13–15]. While we do observe a local temperature rise inside the shear band (both when the system is coupled to a thermostat of a finite relaxation time, as in the simulations reported in this work, and in simulations without thermostatting, not reported here), veinlike patterns do not emerge. We suspect that this is the case due to the limited size of our computer samples. Indeed, the heat generated during failure is expected to be proportional to the elastic energy stored (and subsequently released) in the system and thus finite size effects are expected.

Our next goal is to investigate the spatiotemporal interplay between shear-driven plasticity and dilation-driven void formation inside the glass prior to—and approaching—material failure. In Fig. 3(a), we present a sketch of a rod under tension, illustrating the coexistence of shear-driven plastic events (red) and dilation-driven void formation (blue); see also sketches in the rectangles on the right. As material failure is accompanied by decohesion and the creation of internal free surfaces that cannot sustain stress, we focus on the largest cavity (a cluster of coalesced voids) as a representative indicator of material decohesion under tension, in particular on its size λ in the tensile direction [see bottom-right panel of Fig. 3(a)]. Shear-driven plasticity is monitored based on the best fit of the nonaffine displacement using the common $D^2_{\min}$ field defined in [27]. We detect the nucleation of voids by inserting ghost particles such as done, e.g., in [28,29]. Details are provided in [11].

In Fig. 3(b), we present the evolution of λ with strain ϵ for various T's. Focusing first on the largest T presented [corresponding to the next-to-rightmost sample in Fig. 3(e)], we observe that λ increases with ϵ rather smoothly until a large, discrete/discontinuous jump takes place (marked by the

two arrows). This jump corresponds to the coalescence of two (or more) mesoscopic cavities (see [11]), yet it does not lead to global failure. Instead, λ continues to increase rather smoothly until global failure occurs, defined by $\lambda = \lambda_F$ (marked on the figure by a black circle). We associate the smooth increase in λ with void growth facilitated by shear-driven plasticity, i.e., the plastic expansion of a single cavity within the glass [6,30]. Interestingly, after failure, cavities of finite size λ_R remain locked-in inside the glass, exactly as observed experimentally in Fig. 1(b) (next-to-leftmost panel). As T is decreased, $\lambda(\epsilon)$ features similar properties, yet it is pushed to lower strains and smaller values of λ_F. At the lowest T, failure becomes very abrupt, associated with a rapid (in strain ϵ) formation of a system-spanning (in the diameter direction) cavity, essentially a crack.

In Fig. 3(c), we focus on λ_F as an important quantifier of the overall failure process. In particular, λ_F is plotted as a function of T, for different D_0's. For all D_0's, $\lambda_F(T)$ is nonmonotonic, featuring low values of λ_F for both low and high T (approaching T_g), reaching a maximum at an intermediate T. To shed additional light on this result, we present in Fig. 3(e) snapshots of samples deformed at different T's, at their failure strain [i.e., corresponding to the strain defining λ_F in panel (b)]. In these snapshots (and in the tensile test simulations leading to them), we spatiotemporally tracked shear-driven plasticity (red) and dilation-driven void formation (blue) at the particle level (as explained in [11]), to gain insight into their collective evolution and mutual interactions.

At all T's, shear-driven plasticity takes place first and dilation-driven void formation follows in spatial locations where shear-driven plasticity already took place, suggesting a causal relation between the two basic processes. These observations indicate that shear-driven plasticity leads to the softening of glassy structures [31–33], which in turn apparently reduces typical barriers for void formation [33]. The microscopic mechanism for this coupling between shear-driven plasticity and void formation might be the (transient or persistent) creation of free volume. That is, shear-driven plasticity is known to be accompanied by free-volume creation (see, for example, the recent experiments on colloidal glasses [34,35], which echo similar observations in metallic glasses [36]), and regions of higher free volume might be more susceptible to void formation.

Yet, free-volume creation should be distinguished from void formation, and in particular from cavitation, as the latter involves the formation of new surfaces within the glass (i.e., it involves surface energies) and is influenced by the hydrostatic tension (i.e., the trace of the stress tensor) [37–40]. The hydrostatic tension, in turn, is also reduced through stress relaxation mediated by shear-driven plasticity. Yet another factor at play is the geometric reduction in the cross section of the rod, driven by shear-driven plasticity (which gives rise to the development of a neck at relatively high T), leading to an increase in the local tensile stress. With these interrelated and intrinsically coupled physical processes in mind, we now aim at rationalizing the main observations in Figs. 3(c) and 3(e).

At low T, shear-driven plasticity is localized into a narrow shear band, without any appreciable reduction in the rod's cross section [cf. Fig. 2(c)] and without significant stress relaxation, leading to high tensile stresses [cf. Fig. 2(a)]. Consequently, voids form inside the shear band and rapidly transform into a catastrophic crack under the high tension [41–44], without significantly growing in the tensile direction; hence λ_F is small in this low T regime [cf. Fig. 3(c)]. Note, however, that the number of independent cavities grows with the volume of the shear band and thus scales with D_0^2 (see [11]). We find that the cluster distributions are consistent with the picture provided by homogeneous nucleation theory, with cavitation barriers of only a few $k_B T$ (see [11]), as already pointed out in [45].

With growing T, shear-driven plasticity is more diffused. Moreover, it evolves over larger strain intervals and leads to the reduction in the tensile stress, allowing voids to nucleate, grow, and coalesce. This leads to larger cavities at failure; hence λ_F increases with T in Fig. 3(c). The larger λ_F values manifest themselves as "cup" structures on the fracture surface; see Figs. 2(b) and 2(f) for the relevant simulational results and Fig. 1(b) for the corresponding experimental observations. The larger λ_F values are also accompanied, in this T regime, by residual cavities within the glass; cf. the finite value of λ_R in Fig. 3(b) and the arrows in Fig. 3(e). Finally, while shear-driven plasticity is more diffused in this T regime, shear localization still takes place [possibly along two major orientations; cf. Fig. 3(e) with $T/T_g = 0.386$], leading to a "cone" structure close to the periphery of the failed samples.

As T is further increased, shear-driven plasticity becomes spatially extended, leading to a reduction in both the overall tensile stress and in the rod's local cross section as global failure is approached. The reduction in the tensile stress leads to decreasing values of λ_F, making $\lambda_F(T)$ nonmonotonic. The geometric reduction of the cross section as a neck is formed apparently maintains the local tensile stress sufficiently large to keep λ_F finite. The spatially extended, even more diffused, nature of shear-driven plasticity in this regime also leads to the disappearance of the cone structure. As T is further increased, stress relaxation by shear-driven plasticity accompanying necking is so efficient that cavities cannot grow anymore and λ_F becomes vanishingly small, consistent with the absence of bulk cavities in the experimental data shown on the leftmost part of Fig. 1(b).

The nonmonotonic behavior of $\lambda_F(T)$ is fully consistent with the decrease in the dimple area fraction with increasing σ_{UTS}—corresponding to decreasing T—in the experimental data of Fig. 1(c) and with the decrease in the maximal dimple size with increasing σ_{UTS} in Fig. 1(d). In fact, it predicts that fractographic measurements of the maximal dimple size for σ_{UTS} below 800 MPa will reveal a peak, before dropping. To further connect our simulational findings to the experimental data, which feature significantly larger length scales as discussed above, we present in Fig. 3(d) both λ_F and λ_R as a function of the rod's diameter D_0. Both quantities follow a linear relation with D_0, where for the former we have $\lambda_F \simeq D_0/10$. Extrapolating this result to the experimental length scale, where D_0 is in the mm range, we expect λ_F to be in the 10^{-1} mm range, in the right ballpark of the data presented in Fig. 1(d).

In summary, by combining extensive experiments on metallic glasses and large-scale molecular dynamic simulations of computer glasses, we provided physical insight into the transition in tensile failure modes of glasses, from

necking-mediated failure to shear-banding-mediated failure, as a function of the applied strain rate $\dot{\epsilon}$ and the temperature T. At the macroscopic level, we showed that the sequence of global failure modes depends in a unified manner on the ultimate tensile strength $\sigma_{\mathrm{UTS}}(\dot{\epsilon}, T)$. At the mesoscopic level, using experimental fractography and postmortem sample polishing, as well as particle-scale quantification of computer simulations, we showed that the interplay between shear-driven plasticity and dilation-driven void formation controls the global failure mode.

More specifically, we showed that the spatiotemporal evolution of shear-driven plasticity and dilation-driven void formation—and their intrinsic coupling in space and time—account for the temperature and strain-rate dependence of tensile failure modes in glasses. Our large-scale computer simulations demonstrate that the above mentioned interplay can be quantified through the size of the largest cavity (a cluster of coalesced voids) in the tensile direction, which exhibits a nonmonotonic temperature dependence. Furthermore, we show that the latter scales linearly with the glass sample's diameter, which upon extrapolation offers a possible way to bridge the vast difference in length scales between computer and laboratory glasses.

Our results also pose various questions for future investigations. Among these, we would like to highlight the need to determine whether the transition between the various macroscopic failure modes as a function of temperature and strain rate is continuous or discontinuous and the need to understand the effect of the initial nonequilibrium glass state (fictive temperature), which was kept fixed in this study, on the failure mode. Finally, our results highlight the pressing need to develop elastoplastic constitutive models of glassy deformation, which self-consistently account for both shear- and dilation-driven spatiotemporal, dissipative dynamics.

D.R. acknowledges support from the European Union's Horizon 2020 research and innovation programme under the Marie Sklodowska-Curie grant agreement No. 101024057. This work was performed using HPC resources from GENCI-IDRIS (Grant 2022-AD010913428). E.B. acknowledges support from the Ben May Center for Chemical Theory and Computation and the Harold Perlman Family. E.L. acknowledges support by the National Science Foundation Graduate Research Fellowship under Grant No. 2139841. The experimental work was supported by the Office of Naval Research under Grant No. N00014-20-1-2200.

[1] F. Spaepen, A microscopic mechanism for steady state inhomogeneous flow in metallic glasses, Acta Metall. **25**, 407 (1977).

[2] J. Lu, G. Ravichandran, and W. L. Johnson, Deformation behavior of the $Zr_{41.2}Ti_{13.8}Cu_{12.5}Ni_{10}Be_{22.5}$ bulk metallic glass over a wide range of strain-rates and temperatures, Acta Mater. **51**, 3429 (2003).

[3] G. Wang, J. Shen, J. Sun, Z. Lu, Z. Stachurski, and B. Zhou, Tensile fracture characteristics and deformation behavior of a Zr-based bulk metallic glass at high temperatures, Intermetallics **13**, 642 (2005).

[4] A. H. Vormelker, O. Vatamanu, L. Kecskes, and J. Lewandowski, Effects of test temperature and loading conditions on the tensile properties of a Zr-based bulk metallic glass, Metall. Mater. Trans. A **39**, 1922 (2008).

[5] J. Schroers and W. L. Johnson, Ductile Bulk Metallic Glass, Phys. Rev. Lett. **93**, 255506 (2004).

[6] E. Bouchbinder, T.-S. Lo, I. Procaccia, and E. Shtilerman, Stability of an expanding circular cavity and the failure of amorphous solids, Phys. Rev. E **78**, 026124 (2008).

[7] E. Bouchaud, D. Boivin, J.-L. Pouchou, D. Bonamy, B. Poon, and G. Ravichandran, Fracture through cavitation in a metallic glass, Europhys. Lett. **83**, 66006 (2008).

[8] M. Jiang, Z. Ling, J. Meng, and L. Dai, Energy dissipation in fracture of bulk metallic glasses via inherent competition between local softening and quasi-cleavage, Philos. Mag. **88**, 407 (2008).

[9] E. Bouchbinder, T.-S. Lo, and I. Procaccia, Dynamic failure in amorphous solids via a cavitation instability, Phys. Rev. E **77**, 025101(R) (2008).

[10] J. Ketkaew, W. Chen, H. Wang, A. Datye, M. Fan, G. Pereira, U. D. Schwarz, Z. Liu, R. Yamada, W. Dmowski *et al.*, Mechanical glass transition revealed by the fracture toughness of metallic glasses, Nat. Commun. **9**, 3271 (2018).

[11] See Supplemental Material at http://link.aps.org/supplemental/10.1103/PhysRevMaterials.7.L032601 for technical details about both the experiments and the simulations, along with some additional supporting results, which includes Refs. [10,18–20,25,27,37,43,45–51].

[12] F. Spaepen, On the fracture morphology of metallic glasses, Acta Metall. **23**, 615 (1975).

[13] A. Argon and M. Salama, The mechanism of fracture in glassy materials capable of some inelastic deformation, Mater. Sci. Eng. **23**, 219 (1976).

[14] R. Qu, M. Stoica, J. Eckert, and Z. Zhang, Tensile fracture morphologies of bulk metallic glass, J. Appl. Phys. **108**, 063509 (2010).

[15] R. Qu and Z. Zhang, Compressive fracture morphology and mechanism of metallic glass, J. Appl. Phys. **114**, 193504 (2013).

[16] J. Pan, Y. Wang, and Y. Li, Ductile fracture in notched bulk metallic glasses, Acta Mater. **136**, 126 (2017).

[17] X. K. Xi, D. Q. Zhao, M. X. Pan, W. H. Wang, Y. Wu, and J. J. Lewandowski, Fracture of Brittle Metallic Glasses: Brittleness or Plasticity, Phys. Rev. Lett. **94**, 125510 (2005).

[18] D. Richard, E. Lerner, and E. Bouchbinder, Brittle-to-ductile transitions in glasses: Roles of soft defects and loading geometry, MRS Bull. **46**, 902 (2021).

[19] Y. Shi, Size-independent shear band formation in amorphous nanowires made from simulated casting, Appl. Phys. Lett. **96**, 121909 (2010).

[20] S. Plimpton, Fast parallel algorithms for short-range molecular dynamics, J. Comput. Phys. **117**, 1 (1995).

[21] H. Guo, P. Yan, Y. Wang, J. Tan, Z. Zhang, M. Sui, and E. Ma, Tensile ductility and necking of metallic glass, Nat. Mater **6**, 735 (2007).
[22] C. Volkert, A. Donohue, and F. Spaepen, Effect of sample size on deformation in amorphous metals, J. Appl. Phys. **103**, 083539 (2008).
[23] D. Jang and J. R. Greer, Transition from a strong-yet-brittle to a stronger-and-ductile state by size reduction of metallic glasses, Nat. Mater. **9**, 215 (2010).
[24] D. Magagnosc, R. Ehrbar, G. Kumar, M. He, J. Schroers, and D. Gianola, Tunable tensile ductility in metallic glasses, Sci. Rep. **3**, 1096 (2013).
[25] S. Bonfanti, E. E. Ferrero, A. L. Sellerio, R. Guerra, and S. Zapperi, Damage accumulation in silica glass nanofibers, Nano Lett. **18**, 4100 (2018).
[26] Y. Shi, Size-dependent mechanical responses of metallic glasses, Int. Mater. Rev. **64**, 163 (2019).
[27] M. L. Falk and J. S. Langer, Dynamics of viscoplastic deformation in amorphous solids, Phys. Rev. E **57**, 7192 (1998).
[28] G. Menzl, M. A. Gonzalez, P. Geiger, F. Caupin, J. L. Abascal, C. Valeriani, and C. Dellago, Molecular mechanism for cavitation in water under tension, Proc. Natl. Acad. Sci. USA **113**, 13582 (2016).
[29] B. Galimzyanov and A. Mokshin, Cavity nucleation in single-component homogeneous amorphous solids under negative pressure, J. Phys.: Condens. Matter **34**, 414001 (2022).
[30] X. Tang, T. Nguyen, X. Yao, and J. W. Wilkerson, A cavitation and dynamic void growth model for a general class of strain-softening amorphous materials, J. Mech. Phys. Solids **141**, 104023 (2020).
[31] J. Lewandowski and A. Greer, Temperature rise at shear bands in metallic glasses, Nat. Mater. **5**, 15 (2006).
[32] R. M. O. Mota, E. T. Lund, S. Sohn, D. J. Browne, D. C. Hofmann, S. Curtarolo, A. van de Walle, and J. Schroers, Enhancing ductility in bulk metallic glasses by straining during cooling, Commun. Mater **2**, 23 (2021).
[33] C. Liu, V. Roddatis, P. Kenesei, and R. Maaß, Shear-band thickness and shear-band cavities in a Zr-based metallic glass, Acta Mater. **140**, 206 (2017).
[34] Y. Z. Lu, M. Q. Jiang, X. Lu, Z. X. Qin, Y. J. Huang, and J. Shen, Dilatancy of Shear Transformations in a Colloidal Glass, Phys. Rev. Appl. **9**, 014023 (2018).
[35] X. J. Wang, Y. Z. Lu, X. Lu, J. T. Huo, Y. J. Wang, W. H. Wang, L. H. Dai, and M. Q. Jiang, Elastic criterion for shear-banding instability in amorphous solids, Phys. Rev. E **105**, 045003 (2022).
[36] D. Klaumünzer, A. Lazarev, R. Maaß, F. H. Dalla Torre, A. Vinogradov, and J. F. Löffler, Probing Shear-Band Initiation in Metallic Glasses, Phys. Rev. Lett. **107**, 185502 (2011).
[37] P. Murali, T. F. Guo, Y. W. Zhang, R. Narasimhan, Y. Li, and H. J. Gao, Atomic Scale Fluctuations Govern Brittle Fracture and Cavitation Behavior in Metallic Glasses, Phys. Rev. Lett. **107**, 215501 (2011).
[38] C. H. Rycroft and E. Bouchbinder, Fracture Toughness of Metallic Glasses: Annealing-Induced Embrittlement, Phys. Rev. Lett. **109**, 194301 (2012).
[39] P. Guan, S. Lu, M. J. B. Spector, P. K. Valavala, and M. L. Falk, Cavitation in Amorphous Solids, Phys. Rev. Lett. **110**, 185502 (2013).
[40] M. Vasoya, C. H. Rycroft, and E. Bouchbinder, Notch Fracture Toughness of Glasses: Dependence on Rate, Age, and Geometry, Phys. Rev. Appl. **6**, 024008 (2016).
[41] M. Falk, Molecular-dynamics study of ductile and brittle fracture in model noncrystalline solids, Phys. Rev. B **60**, 7062 (1999).
[42] P. Murali, R. Narasimhan, T. Guo, Y. Zhang, and H. Gao, Shear bands mediate cavitation in brittle metallic glasses, Scr. Mater. **68**, 567 (2013).
[43] J. Luo and Y. Shi, Tensile fracture of metallic glasses via shear band cavitation, Acta Mater. **82**, 483 (2015).
[44] Y. Shao, G.-N. Yang, K.-F. Yao, and X. Liu, Direct experimental evidence of nano-voids formation and coalescence within shear bands, Appl. Phys. Lett. **105**, 181909 (2014).
[45] W. J. Wright, T. Hufnagel, and W. Nix, Free volume coalescence and void formation in shear bands in metallic glass, J. Appl. Phys. **93**, 1432 (2003).
[46] E. Lerner, Mechanical properties of simple computer glasses, J. Non-Cryst. Solids **522**, 119570 (2019).
[47] Y. Shi, Creating atomic models of brittle glasses for in silico mechanical tests, Int. J. Appl. Glass Sci. **7**, 464 (2016).
[48] K. Zhao, Y.-J. Wang, and P. Cao, Fracture universality in amorphous nanowires, J. Mech. Phys. Solids **173**, 105210 (2023).
[49] Y. He, P. Yi, and M. L. Falk, Critical Analysis of an FeP Empirical Potential Employed to Study the Fracture of Metallic Glasses, Phys. Rev. Lett. **122**, 035501 (2019).
[50] X. Tang, L. Shen, H. Zhang, W. Li, and W. Wang, Crack tip cavitation in metallic glasses, J. Non-Cryst. Solids **592**, 121762 (2022).
[51] A. Păduraru, U. G. Andersen, A. Thyssen, N. Bailey, K. W. Jacobsen, and J. Schiøtz, Computer simulations of nanoindentation in Mg–Cu and Cu–Zr metallic glasses, Model. Simul. Mater. Sci. Eng. **18**, 055006 (2010).